CHALMERS

Elasto-plastic crack growth in rails based on material forces

JIM BROUZOULIS

Department of Applied Mechanics
Division of Material and Computational Mechanics
CHALMERS UNIVERSITY OF TECHNOLOGY
Göteborg, Sweden 2012

TECHNICAL REPORT IN SOLID AND STRUCTURAL MECHANICS

Elasto-plastic crack growth in rails based on material forces

JIM BROUZOULIS

Department of Applied Mechanics
Division of Material and Computational Mechanics
CHALMERS UNIVERSITY OF TECHNOLOGY

Göteborg, Sweden 2012

Elasto-plastic crack growth in rails based on material forces
JIM BROUZOULIS

Technical report 2012:04
ISSN 1652-8549
Department of Applied Mechanics
Division of Material and Computational Mechanics
Chalmers University of Technology
SE-412 96 Göteborg
Sweden
Telephone: +46 (0)31-772 1000

Chalmers Reproservice
Göteborg, Sweden 2012

Elasto-plastic crack growth in rails based on material forces
Technical report in Solid and Structural Mechanics
JIM BROUZOULIS
Department of Applied Mechanics
Division of Material and Computational Mechanics
Chalmers University of Technology

Abstract

This report investigates the behaviour of a generalized crack driving force under various loading conditions and for three different material behaviours: elastic; mixed isotropic and kinematic hardening; and nonlinear kinematic hardening with saturation. It is shown that the crack driving force, as derived in this paper, may lead to mesh dependent results for inelastic material behaviour under RCF loading conditions. Therefore, it is not a suitable quantity to use in simulations of crack growth in rails.

Keywords: Material forces, RCF, crack propagation, plasticity

Acknowledgements

This work was performed as part of the activities within the Centre of Excellence CHARMEC (CHAlmers Railway Mechanics, `www.charmec.chalmers.se`). The author would also like to acknowledge professor Magnus Ekh (Applied Mechanics, Chalmers University of Technology) for many rewarding discussions.

Contents

Abstract i

Acknowledgements i

Contents iii

1 Introduction 1

2 Material forces and RCF 1
2.1 Governing equations . . . 1
2.2 Kinematics . . . 1
2.3 Energy Balance - Dissipation of Energy . . . 2
2.4 Crack Driving Force - Eshelby Stress . . . 4
2.5 Choice of Weight Function . . . 5

3 FE model of rail with a crack 5
3.1 Material model . . . 7

4 Discretization studies 8
4.1 Alternating tension–compression . . . 8
4.1.1 Elasticity . . . 8
4.1.2 Linear mixed hardening . . . 8
4.2 RCF loading . . . 9
4.2.1 Elasticity–inclined crack ($\varphi = 20°$) . . . 9
4.2.2 Linear mixed hardening – inclined crack ($\varphi = 20°$) . . . 10
4.2.3 Nonlinear kinematic hardening – inclined crack ($\varphi = 20°$) . . . 11
4.2.4 Nonlinear kinematic hardening – vertical crack ($\varphi = 90°$) . . . 12
4.2.5 Crack growth direction . . . 13
4.3 Time discretization . . . 14

5 Concluding remarks and outlook 15

References 15

1 Introduction

Rolling Contact Fatigue (RCF) of rails are major problems in the railway industry due to safety concerns and high costs associated with maintenance, cf. [6]. Therefore, being able to predict the service life of rails is of high value as it allows for optimization; not only in terms of maintenance but also (re)investments in the infrastructure.

The development of tools for life prediction of rails must include models for the growth of cracks and in relation to this topic much research has been carried out on the vast topic of RCF, see for example the overview by Ekberg et al. [3]. As a step towards the development of the aforementioned tools, the current paper presents a numerical FE model for 2D simulation of head-check like crack growth in rails.

The framework is based on the concept of material forces which are here used to characterise the state at the crack tip through the evaluation of a *generalized crack driving force*, $\boldsymbol{\mathcal{G}}$. It is of considerable interest to assess how inelastic material behaviour affects crack growth; especially for rails which undergoes large plastic deformation at the rail surface where also many cracks initiate. To this end, the current study investigates the behaviour of $\boldsymbol{\mathcal{G}}$ for three different material behaviours: elastic; mixed isotropic and kinematic hardening; and nonlinear kinematic hardening with saturation.

2 Material forces and RCF

In this section a framework for computation of the rate of energy dissipation (also known as the energy release rate), based on the concept of material forces, is presented. This formulation results in a vectorial crack driving force $\boldsymbol{\mathcal{G}}$ which is energy conjugated to the crack tip velocity. This quantity is then a suitable quantity for formulation of a propagation law.

2.1 Governing equations

What follows is a summary of the governing equations for the generalized crack driving force for a inhomogeneous dissipative material, cf. [8, 7, 5]:

$$\begin{aligned}\boldsymbol{\mathcal{G}} =& \boldsymbol{\mathcal{G}}_{\text{int}} + \boldsymbol{\mathcal{G}}_{\text{vol}} + \boldsymbol{\mathcal{G}}_{\text{sur}} \\ =& \int_{\mathcal{B}_{\text{X}}} -\boldsymbol{\Sigma} \cdot (W \boldsymbol{\nabla}_{\text{X}}) \mathrm{d}V_{\text{X}} + \int_{\mathcal{B}_{\text{X}}} W \boldsymbol{B}_{\text{X}} \mathrm{d}V_{\text{X}} + \int_{\partial\mathcal{B}_{\text{X}}} W \boldsymbol{\Sigma} \cdot \boldsymbol{N} \mathrm{d}S_{\text{X}}\end{aligned} \tag{2.1}$$

where $\boldsymbol{\Sigma}$ is the Eshelby stress tensor, defined as

$$\boldsymbol{\Sigma} = \psi_{\text{X}} \boldsymbol{I} - \boldsymbol{F}^{\text{T}} \boldsymbol{P} \tag{2.2}$$

with the strain energy ψ_{X}, deformation gradient $\boldsymbol{F}$ and first Piola-Kirchhoff stress tensor $\boldsymbol{P}$. In addition the configurational body force $\boldsymbol{B}_{\text{X}}$ is defined as

$$\boldsymbol{B}_{\text{X}} = -\boldsymbol{K} \circ \boldsymbol{\nabla}_{\text{X}} \boldsymbol{k} - \boldsymbol{\nabla}_{\text{X}} \psi_{\text{X}} - \boldsymbol{F}^{\text{T}} \boldsymbol{b}_{\text{X}} \tag{2.3}$$

and the configurational surface traction $\boldsymbol{T}_{\text{X}}$

$$\boldsymbol{T}_{\text{X}} = -\boldsymbol{F}^{\text{T}} \boldsymbol{t}_{\text{X}} \tag{2.4}$$

The term $\boldsymbol{K} \circ \boldsymbol{\nabla}_{\text{X}} \boldsymbol{k}$ is the contribution due to changes of the internal variables caused by changes in the configuration and $\boldsymbol{\nabla}_{\text{X}} \psi_{\text{X}}$ is due to inhomogeneities in the material. Finally, $\boldsymbol{b}_{\text{X}}$ and $\boldsymbol{t}_{\text{X}}$ is the volume force and surface traction, in the reference configuration, respectively. The domain of the body is denoted $\mathcal{B}_{\text{X}}$ and the boundary is denoted $\partial\mathcal{B}_{\text{X}}$ with the unit normal $\boldsymbol{N}$. In eq. (2.1), W is a weight function with local support around the crack tip, see section 2.5 for details.

2.2 Kinematics

Following the steps of [8], we first consider the spatial motion problem, c.f. Fig. 2.1 which is expressed in a standard way through the motion map $\boldsymbol{x} = \boldsymbol{\varphi}(\boldsymbol{X}, t)$. Here the material particles in the reference configuration,

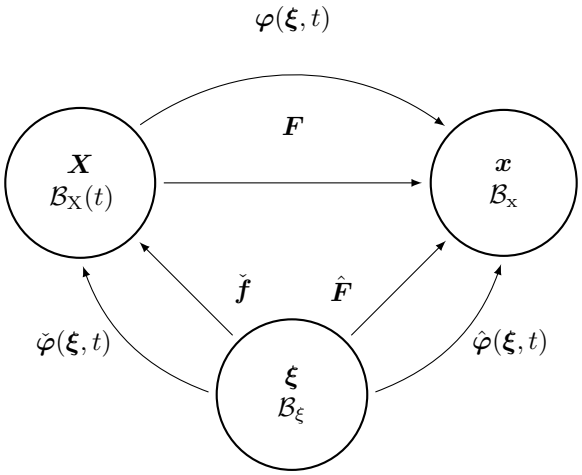

Figure 2.1: *Current, reference and absolute reference configuration.*

$\boldsymbol{X}$, are mapped to the current configuration, $\boldsymbol{x} \in \mathcal{B}_{\mathrm{x}}(t)$. Now consider a third configuration, the so called absolute reference configuration, B_{ξ} which is fixed w.r.t. time. By introducing this fixed configuration the reference configuration is allowed to change with time, expressed through the absolute material map $\boldsymbol{X} = \check{\boldsymbol{\varphi}}(\boldsymbol{\xi}, t) \in \mathcal{B}_{\mathrm{X}}(t)$. Next define an absolute spatial motion map, $\boldsymbol{x} = \hat{\boldsymbol{\varphi}}(\boldsymbol{\xi}, t)$, between the absolute reference configuration and the current configuration.

The introduction of an extra configuration, $\mathcal{B}_{\xi}$, allows the change in energy due to changes of the (reference) configuration to be evaluated. This is of outermost importance in the case of a propagating crack, as the reference configuration is continuously changing.

For each mapping a pertinent deformation gradient can be defined. For the spatial motion we have $\boldsymbol{F} = \boldsymbol{\varphi}(\boldsymbol{X}, t) \otimes \boldsymbol{\nabla}_{\mathrm{X}}$, and analogously for the absolute material motion $\check{\boldsymbol{F}} = \check{\boldsymbol{\varphi}}(\boldsymbol{\xi}, t) \otimes \boldsymbol{\nabla}_{\xi}$. The deformation gradient for the absolute spatial motion $\hat{\boldsymbol{F}}$, can be obtained from the composite map, $\check{\boldsymbol{\varphi}}(\boldsymbol{\xi}, t) = (\boldsymbol{\varphi} \circ \check{\boldsymbol{\varphi}})(\boldsymbol{X}, t)$, as

$$\hat{\boldsymbol{F}} = \boldsymbol{F}\check{\boldsymbol{F}} \tag{2.5}$$

2.3 Energy Balance - Dissipation of Energy

Following the outline of [4] a thermodynamically consistent crack driving force is derived. For later use the weak form of momentum balance (in the reference configuration) is introduced as

$$\int_{\mathcal{B}_{\mathrm{X}}} \boldsymbol{P} : [\delta\dot{\boldsymbol{x}} \otimes \boldsymbol{\nabla}_{\mathrm{X}}] \mathrm{d}V_{\mathrm{X}} = \int_{\mathcal{B}_{\mathrm{X}}} \boldsymbol{b}_{\mathrm{X}} \cdot \delta\dot{\boldsymbol{x}} \mathrm{d}S_{\mathrm{X}} + \int_{\partial\mathcal{B}_{\mathrm{X}}} \boldsymbol{t}_{\mathrm{X}} \cdot \delta\dot{\boldsymbol{x}} \mathrm{d}S_{\mathrm{X}} \tag{2.6}$$

According to the first law of thermodynamics the total balance of energy in the case of quasi static isothermal processes, can be written

$$\frac{\mathrm{d}}{\mathrm{d}t}[\mathcal{E} + \Gamma] = \mathcal{W} \tag{2.7}$$

where $\mathcal{E}$ is the total internal energy of the body, defined as

$$\mathcal{E} = \int_{\mathcal{B}_{\mathrm{X}}} e_{\mathrm{X}} \mathrm{d}V_{\mathrm{X}} \tag{2.8}$$

with e_{X} being the (volume specific) internal energy density which may be split (additively) into a free (strain energy) and a non-free (dissipative) part respectively, according to

$$e_{\mathrm{X}} = \psi_{\mathrm{X}} + \upsilon_{\mathrm{X}} \tag{2.9}$$

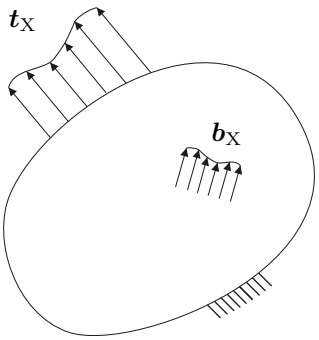

Figure 2.2: Energy quantities associated with the body.

In addition, the corresponding global quantities to the equation above may be introduced such that the total internal energy $\mathcal{E}$ can be expressed

$$\mathcal{E} = \Psi + \Upsilon \tag{2.10}$$

where Ψ is the Helmholz free energy, given as

$$\Psi = \int_{\mathcal{B}_{\mathrm{X}}} \psi_{\mathrm{X}} \mathrm{d}V_{\mathrm{X}} \tag{2.11}$$

and Υ is the dissipative energy of the body

$$\Upsilon = \int_{\mathcal{B}_{\mathrm{X}}} \upsilon_{\mathrm{X}} \mathrm{d}V_{\mathrm{X}} \tag{2.12}$$

Moreover, in equation (2.7), the crack surface energy Γ has been introduced as

$$\Gamma = \int_{\partial\mathcal{B}_{\mathrm{X}}} \gamma_{\mathrm{X}} \mathrm{d}S_{\mathrm{X}} \tag{2.13}$$

with the surface energy density γ_{X} which describes the amount of stored energy on the boundary of potential crack surfaces. Furthermore, the mechanical power input $\mathcal{W}$, which is the work of all external forces, is expressed in a standard way.

$$\mathcal{W} = \int_{\mathcal{B}_{\mathrm{X}}} \boldsymbol{b}_{\mathrm{X}} \cdot \boldsymbol{v} \mathrm{d}V_{\mathrm{X}} + \int_{\partial\mathcal{B}_{\mathrm{X}}} \boldsymbol{t}_{\mathrm{X}} \cdot \boldsymbol{v} \mathrm{d}S_{\mathrm{X}} \tag{2.14}$$

where $\boldsymbol{v}$ is the spatial velocity field.

Next, a rate of dissipation functional $\mathcal{D}$ is introduced as the total time rate of change of the (global) dissipative part of the internal energy, which according to the second law of thermodynamics always must be non-negative.

$$\mathcal{D} = \frac{\mathrm{d}}{\mathrm{d}t}\Upsilon \geq 0 \tag{2.15}$$

The expression above combined with equation (2.7) and (2.10) can be written

$$\mathcal{D} = \mathcal{W} - \frac{\mathrm{d}}{\mathrm{d}t}[\Psi + \Gamma] \tag{2.16}$$

By introducing a specific (additive) split, for the rate of dissipation above, into a driving and a resisting part one obtains

$$\mathcal{D} = \mathcal{D}_{\mathrm{drive}} - \mathcal{D}_{cr} \geq 0 \tag{2.17}$$

where we have introduced the $\mathcal{D}_{\mathrm{drive}}$ pertaining to energy release due to changes in the configuration (only), given as

$$D_{\mathrm{drive}} = \mathcal{W} - \frac{\mathrm{d}}{\mathrm{d}t}\Psi \tag{2.18}$$

and the global crack resistance $\mathcal{D}_{cr}$ expressed as

$$\mathcal{D}_{cr} = \frac{\mathrm{d}}{\mathrm{d}t}\Gamma \tag{2.19}$$

which is related to the fracture toughness encountered in classical fracture mechanics.

2.4 Crack Driving Force - Eshelby Stress

In order to obtain a more (computationally) useful expression for the energy dissipation we make use of a generalized *Reynold's transport theorem*, cf. [4].

$$\frac{\mathrm{d}}{\mathrm{d}t}\mathcal{F} = \int_{\mathcal{B}_\mathrm{X}} [\mathrm{D}_\mathrm{t} f + [f\dot{\boldsymbol{X}}] \cdot \boldsymbol{\nabla}_\mathrm{X}] \mathrm{d}S_\mathrm{X} \tag{2.20}$$

which contains the non-standard term $[f \otimes \boldsymbol{\nabla}_\mathrm{X}] \cdot \dot{\boldsymbol{X}}$ emanating from the fact that the reference configuration is now time dependent, $\boldsymbol{X} = \boldsymbol{X}(\xi, t)$. Applying equation (2.20) to the definition for the Helmholz free energy in equation (2.11) we obtain

$$\frac{\mathrm{d}}{\mathrm{d}t}\Psi = \int_{\mathcal{B}_\mathrm{X}} [\mathrm{D}_\mathrm{t}\psi_\mathrm{X} + [\psi_\mathrm{X}\dot{\boldsymbol{X}}] \cdot \boldsymbol{\nabla}_\mathrm{X}] \mathrm{d}V_\mathrm{X} = \mathcal{W} + \int_{\mathcal{B}_\mathrm{X}} [\psi_\mathrm{X}\dot{\boldsymbol{X}}] \cdot \boldsymbol{\nabla}_\mathrm{X}\, \mathrm{d}V_\mathrm{X}$$

and thus the rate of mechanical dissipation is reduced to

$$D_\mathrm{drive} = -\int_{\mathcal{B}_\mathrm{X}} [\psi\dot{\boldsymbol{X}}] \cdot \boldsymbol{\nabla}_\mathrm{X}\, \mathrm{d}V_\mathrm{X} \tag{2.21}$$

Note that, this expression only includes dissipation due to configurational changes and the expression inside the integral above is expanded as

$$[\psi_\mathrm{X}\dot{\boldsymbol{X}}] \cdot \boldsymbol{\nabla}_\mathrm{X} = (\psi_\mathrm{X}\, \boldsymbol{\nabla}_\mathrm{X}) \cdot \dot{\boldsymbol{X}} + \psi_\mathrm{X}\boldsymbol{I} : (\dot{\boldsymbol{X}} \otimes \boldsymbol{\nabla}_\mathrm{X}) \tag{2.22}$$

From here on we make an assumption regarding the expression for the free energy ψ_X:

$$\psi_\mathrm{X} = \psi_\mathrm{X}(\boldsymbol{F}, \boldsymbol{k}, \boldsymbol{X}) \tag{2.23}$$

where $\boldsymbol{k}$ denotes an array of internal variables which may represent various dissipative processes. Furthermore an explicit dependence on $\boldsymbol{X}$ has been included in order to account for material inhomogeneities.

With this particular assumption, eq. (2.24) can be written

$$[\psi_\mathrm{X}\dot{\boldsymbol{X}}] \cdot \boldsymbol{\nabla}_\mathrm{X} = \Big[\boldsymbol{P} : (\boldsymbol{F} \otimes \boldsymbol{\nabla}_\mathrm{X}) + \boldsymbol{K} \circ (\boldsymbol{k} \otimes \boldsymbol{\nabla}_\mathrm{X}) + (\psi_\mathrm{X}\, \boldsymbol{\nabla}_\mathrm{X})\Big] \cdot \dot{\boldsymbol{X}} + \psi_\mathrm{X}\boldsymbol{I} : (\dot{\boldsymbol{X}} \otimes \boldsymbol{\nabla}_\mathrm{X}) \tag{2.24}$$

and by noting that

$$(\boldsymbol{F} \otimes \boldsymbol{\nabla}_\mathrm{X}) \cdot \dot{\boldsymbol{X}} = (\boldsymbol{F}\dot{\boldsymbol{X}}) \otimes \boldsymbol{\nabla}_\mathrm{X} - \boldsymbol{F}(\dot{\boldsymbol{X}} \otimes \boldsymbol{\nabla}_\mathrm{X}) \tag{2.25}$$

the rate of mechanical dissipation can be expressed

$$D_\mathrm{drive} = -\int_{\mathcal{B}_\mathrm{X}} \boldsymbol{\Sigma} : (\dot{\boldsymbol{X}} \otimes \boldsymbol{\nabla}_\mathrm{X}) \mathrm{d}V_\mathrm{X} - \int_{\mathcal{B}_\mathrm{X}} \boldsymbol{P} : (\boldsymbol{F}\dot{\boldsymbol{X}}) \otimes \boldsymbol{\nabla}_\mathrm{X}\, \mathrm{d}V_\mathrm{X} - \int_{\mathcal{B}_\mathrm{X}} \Big[\boldsymbol{K} \circ (\boldsymbol{k} \otimes \boldsymbol{\nabla}_\mathrm{X}) + \psi_\mathrm{X}\, \boldsymbol{\nabla}_\mathrm{X}\Big] \cdot \dot{\boldsymbol{X}} \mathrm{d}V_\mathrm{X} \tag{2.26}$$

where we have defined the *Eshelby* stress tensor $\boldsymbol{\Sigma}$ as

$$\boldsymbol{\Sigma} = \psi_\mathrm{X}\boldsymbol{I} - \boldsymbol{F}^\mathrm{T}\boldsymbol{P} \tag{2.27}$$

With the help of the weak form of the momentum balance in equation (2.6) with the *choice* $\delta\boldsymbol{x} = \boldsymbol{F}\dot{\boldsymbol{X}}$ the second term on the right hand side of equation (2.28) may be rewritten as, c.f. [**Tillberg**],

$$\int_{\mathcal{B}_\mathrm{X}} \boldsymbol{P} : (\boldsymbol{F}\dot{\boldsymbol{X}}) \otimes \boldsymbol{\nabla}_\mathrm{X}\, \mathrm{d}V_\mathrm{X} = \int_{\mathcal{B}_\mathrm{X}} \boldsymbol{F}^\mathrm{T}\boldsymbol{b}_\mathrm{X} \cdot \dot{\boldsymbol{X}} \mathrm{d}V_\mathrm{X} + \int_{\partial\mathcal{B}_\mathrm{X}} \boldsymbol{F}^\mathrm{T}\boldsymbol{t}_\mathrm{X} \cdot \dot{\boldsymbol{X}} \mathrm{d}S_\mathrm{X}$$

The dissipation now becomes

$$D_\mathrm{drive} = -\int_{\mathcal{B}_\mathrm{X}} \boldsymbol{\Sigma} : (\dot{\boldsymbol{X}} \otimes \boldsymbol{\nabla}_\mathrm{X}) \mathrm{d}V_\mathrm{X} + \int_{\mathcal{B}_\mathrm{X}} \boldsymbol{B}_\mathrm{X} \cdot \dot{\boldsymbol{X}} \mathrm{d}V_\mathrm{X} + \int_{\partial\mathcal{B}_\mathrm{X}} \boldsymbol{T}_\mathrm{X} \cdot \dot{\boldsymbol{X}} \partial\mathcal{B}_\mathrm{X} \tag{2.28}$$

where $\boldsymbol{B}_\mathrm{X}$ and $\boldsymbol{T}_\mathrm{X}$ is the configurational volume force and configurational surface traction respectively, and are defined as

$$\boldsymbol{B}_\mathrm{X} = -\boldsymbol{K} \circ (\boldsymbol{k} \otimes \boldsymbol{\nabla}_\mathrm{X}) - \psi_\mathrm{X}\, \boldsymbol{\nabla}_\mathrm{X} - \boldsymbol{F}^\mathrm{T}\boldsymbol{b}_\mathrm{X} \tag{2.29}$$

Figure 2.3: Components of the generalized crack driving force.

$$\boldsymbol{T}_{\mathrm{X}} = -\boldsymbol{F}^{\mathrm{T}}\boldsymbol{t}_{\mathrm{X}} \tag{2.30}$$

The expression in eq. 2.28 represents the energy released due to a virtual change of the reference domain. Next the rate of energy dissipation due to a change in configuration $\delta\dot{\boldsymbol{X}}$ in the domain $\mathcal{B}_{\mathrm{X}}$ with boundary $\partial\mathcal{B}_{\mathrm{X}}$ is obtained from equation (2.28) as

$$D(\delta\dot{\boldsymbol{X}}) = -\int_{\mathcal{B}_{\mathrm{X}}} \boldsymbol{\Sigma} : (\delta\dot{\boldsymbol{X}} \otimes \boldsymbol{\nabla}_{\mathrm{X}})\mathrm{d}V_{\mathrm{X}} + \int_{\mathcal{B}_{\mathrm{X}}} \boldsymbol{B}_{\mathrm{X}} \cdot \delta\dot{\boldsymbol{X}}\mathrm{d}V_{\mathrm{X}} + \int_{\partial\mathcal{B}_{\mathrm{X}}} \boldsymbol{T}_{\mathrm{X}} \cdot \delta\dot{\boldsymbol{X}}\partial\mathcal{B}_{\mathrm{X}} \tag{2.31}$$

Now make the *choice* to parameterize the variation $\delta\dot{\boldsymbol{X}}$ through the (virtual) *crack tip velocity* $\delta\dot{\boldsymbol{a}}$

$$\delta\dot{\boldsymbol{X}} = W(\boldsymbol{X})\delta\dot{\boldsymbol{a}} \tag{2.32}$$

where $W(\boldsymbol{X})$ is a suitably chosen scalar valued function. The rate of energy release $\mathcal{G}$ in a region around the crack tip can now be expressed as

$$\mathcal{G}(\delta\dot{\boldsymbol{a}}) = \mathcal{D}(\delta\dot{\boldsymbol{a}}) = \boldsymbol{\mathcal{G}} \cdot \delta\dot{\boldsymbol{a}} \tag{2.33}$$

where we have defined the *generalized crack driving force* (GCDF) $\boldsymbol{\mathcal{G}}$ as the energy conjugate to the crack tip velocity

$$\boldsymbol{\mathcal{G}} = \boldsymbol{\mathcal{G}}_{\mathrm{int}} + \boldsymbol{\mathcal{G}}_{\mathrm{vol}} + \boldsymbol{\mathcal{G}}_{\mathrm{sur}} - \int_{\mathcal{B}_{\mathrm{X}}} \boldsymbol{\Sigma} \cdot (W\,\boldsymbol{\nabla}_{\mathrm{X}})\mathrm{d}V_{\mathrm{X}} + \int_{\mathcal{B}_{\mathrm{X}}} W\boldsymbol{B}_{\mathrm{X}}\mathrm{d}V_{\mathrm{X}} + \int_{\partial\mathcal{B}_{\mathrm{X}}} W\boldsymbol{T}_{\mathrm{X}}\partial\mathcal{B}_{\mathrm{X}} \tag{2.34}$$

By introducing a local coordinate system at the crack tip the crack driving force can be decomposed into two components $\boldsymbol{\mathcal{G}} = \boldsymbol{\mathcal{G}}_{\parallel} + \boldsymbol{\mathcal{G}}_{\perp} = \mathcal{G}_{\parallel} \cdot \boldsymbol{e}_{\parallel} + \mathcal{G}_{\perp} \cdot \boldsymbol{e}_{\perp}$, cf. Fig. 2.3. As pointed out by several authors the parallel component of $\mathcal{G}_{\mathrm{int}}$ is equal to the classical $\mathcal{J}$-integral expressed as a domain integral, i.e. $\boldsymbol{\mathcal{G}}_{\mathrm{int}} \cdot \boldsymbol{e}_{\parallel} = \mathcal{J}$. Analogously to the vectorial driving force a *vectorial crack resistance* can be obtained with the assumption that the material in general is inhomogeneous i.e. $\gamma = \gamma(\boldsymbol{X})$.

$$\mathcal{D}_{cr}(\delta\dot{\boldsymbol{X}}) = \boldsymbol{\mathcal{G}}_{cr} \cdot \delta\dot{\boldsymbol{a}} \tag{2.35}$$

2.5 Choice of Weight Function

When evaluating the energy dissipation, the choice of the scalar function φ in equation (2.32) is arbitrary. However the particular *choice* of φ is still of considerable interest as it describes the material motion near the crack tip. Introduce the specific choice of $\varphi = W(\boldsymbol{X})$, with $W(\boldsymbol{X})$ being a scalar weight function defined over $\mathcal{B}_{\mathrm{X}}$, c.f. Fig. **??**. $W(\boldsymbol{X})$ is chosen to be non-zero only in the domain $\mathcal{B}_{\mathrm{X}}$, which (for simplicity) is constructed to have a circular shape surrounding the crack tip. Moreover, the weight function is chosen to vary linearly from 0 at the boundary $\partial\mathcal{B}_{\mathrm{X}}$, to 1 at the crack tip, $\boldsymbol{X} = \boldsymbol{X}_{cr}$, forming a cone centered at the crack tip. Due to the parameterization of $\partial\dot{\boldsymbol{X}}$ in equation (**??**) this choice of W implies that the domain $\mathcal{B}_{\mathrm{X}}$ around the crack tip is extended in the direction of $\dot{\boldsymbol{a}}$. Expressed in a (r, θ)-polar coordinate system with origin at $\boldsymbol{X} = \boldsymbol{X}_{cr}$, and the boundary $\partial\mathcal{B}_{\mathrm{X}}$ given at a distance $r = R$ from the origin we have, cf. Fig. **??**.

$$W(r) = \begin{cases} 1 - \frac{r}{R} & \text{if} \quad r \leq R \\ 0 & \text{if} \quad r > R \end{cases} \tag{2.36}$$

Where the radius R is considered model parameter.

3 FE model of rail with a crack

The model problem consists of a rectangular section of the rail surface with a single edge crack of initial length a_0 and initial inclination φ_0. In a real rail with head–checks, a single crack is not observed but rather a network of cracks which interact and may give rise to shielding effects, see for example [**Tillberg2009**]. However, the simulations in this study are limited to a two dimensional single crack, due to the increased complexity associated with the simulation of multiple cracks growing simultaneously.

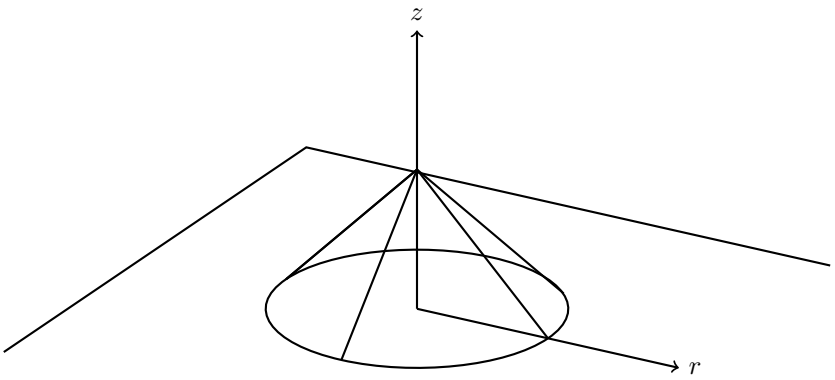

Table 3.1: Geometry parameters and load parameters.

(a)

p_{N} (el)	p_{N} (pl)	h	w	b	a_0	φ_0
1200 MN/m	600 MN/m	40 mm	80 mm	7.4 mm	1 mm	25°

Table 3.2: Material parameters for (a) linear mixed hardening, (b) nonlinear kinematic hardening.

(a)

E	ν	σ_{y}	H_{kin}	H_{iso}	B_∞	K_∞
210 GPa	0.3	500 MPa	$E/8$	$E/8$	∞ MPa	∞ MPa

(b)

E	ν	σ_{y}	H_{kin}	H_{iso}	B_∞	K_∞
210 GPa	0.3	430 MPa	41 GPa	10 GPa	707 MPa	∞ MPa

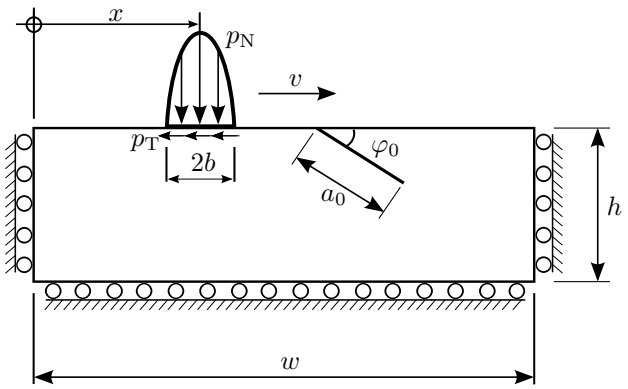

Figure 3.1: *Problem geometry and boundary conditions.*

The material is assumed to be in a state of plane strain, with material and load parameters listed in Table 3.2(a). Constant Strain Triangular (CST) elements have been used to discretize the whole domain and, therefore, a high mesh density is needed around the crack tip in order to capture the high stress and strain gradients. Also note that in order to compute the gradients of the internal variables, the values have been averaged to the nodes.

In this study the number of degrees of freedom are in the range of 20k and each load cycle has been discretized with 100 timesteps. The reader is referred to [1] for further details on the computational mesh and discretization studies.

A contact algorithm, based on a penalty formulation is included in order to avoid penetration of the crack faces. In addition, the crack surfaces are modelled as completely smooth (i.e. no friction) which may correspond to the crack being filled by some fluid (e.g. lubrication). It is often assumed in literature that this fluid becomes entrapped while the wheel passes over the crack mouth. This entrapment then results in pressurization of the crack which increases the load at the crack tip.

3.1 Material model

The material model adopted in this study is the *Chaboche* model for small strains with nonlinear isotropic and kinematic hardening, see [notes from Ekh] for details. Furthermore, the material is assumed homogeneous and isotropic. The free energy can be written

$$\psi_{\mathrm{X}} = \frac{1}{2}\boldsymbol{\epsilon}_{\mathrm{e}} : \boldsymbol{E}_{\mathrm{e}} : \boldsymbol{\epsilon}_{\mathrm{e}} + \frac{1}{2}H_{\mathrm{iso}}k^2 + \frac{1}{3}H_{\mathrm{kin}}|\boldsymbol{\beta}|^2 \tag{3.1}$$

with the elastic strain $\boldsymbol{\epsilon}_{\mathrm{e}} = \boldsymbol{\epsilon} - \boldsymbol{\epsilon}_{\mathrm{p}}$. The internal variables are collected in the array $\boldsymbol{k}$

$$\boldsymbol{k} = \{\boldsymbol{\epsilon}_{\mathrm{p}}, \quad k, \quad \boldsymbol{\beta}\} \tag{3.2}$$

such that the an array of the (energy conjugated) dissipative stresses may be obtained as

$$\boldsymbol{K} = -\frac{\mathrm{d}\,\psi_{\mathrm{X}}}{\mathrm{d}\boldsymbol{k}} = -\left\{\frac{\partial\,\psi_{\mathrm{X}}}{\partial\,\boldsymbol{\epsilon}_{\mathrm{p}}}, \quad \frac{\partial\,\psi_{\mathrm{X}}}{\partial\,k}, \quad \frac{\partial\,\psi_{\mathrm{X}}}{\partial\,\boldsymbol{\beta}}\right\} = \left\{\boldsymbol{\sigma}, \quad -kH_{\mathrm{iso}}, \quad -\frac{2}{3}\boldsymbol{\beta}H_{\mathrm{kin}}\right\} \tag{3.3}$$

Furthermore, the gradients of the internal variables are obtained as

$$\boldsymbol{k} \otimes \boldsymbol{\nabla}_{\mathrm{X}} = \left\{\frac{\partial\,\boldsymbol{\epsilon}_{\mathrm{p}}}{\partial\,\boldsymbol{X}}, \quad \frac{\partial\,k}{\partial\,\boldsymbol{X}}, \quad \frac{\partial\,\boldsymbol{\beta}}{\partial\,\boldsymbol{X}}\right\} \tag{3.4}$$

and thus the configurational volume force may be expressed as

$$\boldsymbol{B}_{\mathrm{X}} = \boldsymbol{\sigma} : \frac{\partial\,\boldsymbol{\epsilon}_{\mathrm{p}}}{\partial\,\boldsymbol{X}} - kH_{\mathrm{iso}}\frac{\partial\,k}{\partial\,\boldsymbol{X}} - \frac{2}{3}H_{\mathrm{kin}}\boldsymbol{\beta} : \frac{\partial\,\boldsymbol{\beta}}{\partial\,\boldsymbol{X}} \tag{3.5}$$

Because CST elements with one integration point have been used in this study the internal variables are averaged at the nodes in order to have a continuous variation over the domain. Thus the

4 Discretization studies

In this section the total material force $\mathcal{G}$ along with its components $\mathcal{G}_{\text{int}}$, $\mathcal{G}_{\text{sur}}$ and $\mathcal{G}_{\text{vol}}$ are presented for different load cases and material models. Note that only the *parallel* component of the material force is presented as it has previously been shown that the *perpendicular* component is non-convergent, cf. [ref]. Two load cases have been studied: alternating tension compression and RCF loading. Furthermore, the material model employed is the so-called Chaboche model where the material parameters have been varied to model different material responses: elastic, linear mixed hardening and nonlinear kinematic hardening. $a_{\text{len}} = 1mm$, $\varphi_0 = \{20,\ 90\}$ deg., $R = 0.2$ mm, $\bar{\epsilon} = 0.2$ mm, $\mu = 0.3$.

4.1 Alternating tension–compression

The plate is subjected to alternating tension according to

$$p_{\text{T}=}p_0 \sin(2\pi t) \qquad t \in [0, 1] \tag{4.1}$$

which results in one opening and one closing cycle of the crack. This simplified load case has been chosen in order to avoid complex loading near the crack introduced by a moving Hertzian load, otherwise typical for RCF loading.

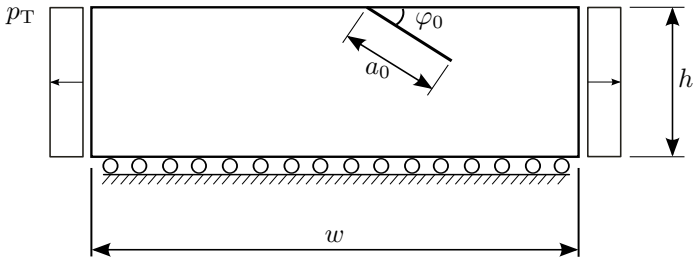

Figure 4.1: *Problem geometry and boundary conditions.*

4.1.1 Elasticity

In figure 4.2 it is seen that $\mathcal{G}_{\text{sur}}$ is close to converge for refined mesh density; however, the magnitudes of $\mathcal{G}_{\text{sur}}$ are small in comparison to $\mathcal{G}_{\text{int}}$ and will, therefore, not influence $\mathcal{G}$ noticeable. Also, as the material behaviour is elastic so $\mathcal{G}_{\text{vol}}$ is zero.

4.1.2 Linear mixed hardening

From figure 4.3 it is seen that $\mathcal{G}_{\text{sur}}$ behaves highly unstable and does not converge with increased mesh density. However, just as in the elastic case the magnitude of $\mathcal{G}_{\text{sur}}$ is small in comparison to $\mathcal{G}_{\text{int}}$. What is also noteworthy is that $\mathcal{G}$ appears more mesh convergent than $\mathcal{G}_{\text{int}}$ and $\mathcal{G}_{\text{sur}}$ individually. This illustrates that the total energy dissipated near the crack tip is constant even though the dissipation contribution from $\mathcal{G}_{\text{int}}$, $\mathcal{G}_{\text{sur}}$ and $\mathcal{G}_{\text{vol}}$ are dependent on the chosen discretization. Therefore; it is concluded that for this simplified load case, $\mathcal{G}$ is mesh independent for sufficiently fine mesh.

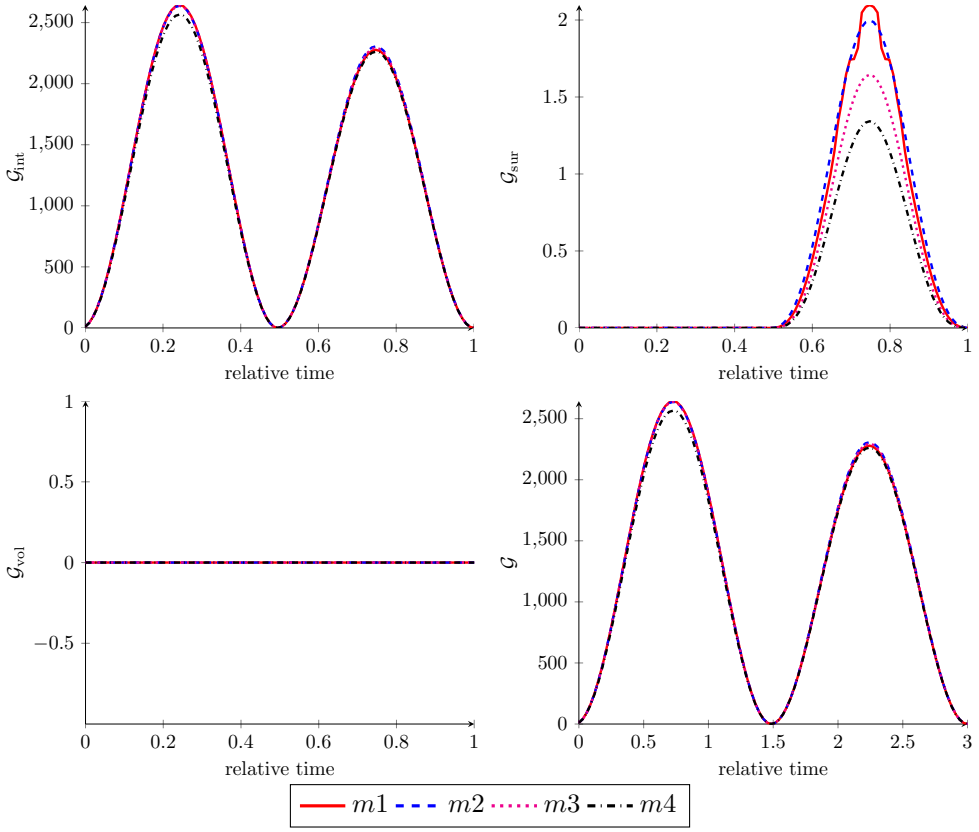

Figure 4.2: *Alternating tension–compression, inclined crack, $a_0 = 1$ mm, $\varphi = 20$ deg. Components of the material force with elastic material behaviour for different mesh densities.*

4.2 RCF loading

In this example, the rail is subjected to a wheel load modelled as a Hertzian load moving over the boundary from left to right and constitutes a simplified RCF loading case. Full slip is assumed between the wheel and rail with a traction force acting to the left. In the subsequent studies, two values for the initial angle have been studied, $\varphi_0 = \{20°,\ 90°\}$.

4.2.1 Elasticity–inclined crack ($\varphi = 20°$)

In figure 4.5 it is again observed that $\mathcal{G}_{\text{sur}}$ is not convergent with respect to mesh density; however, just as in the case for alternating tension the magnitudes of $\mathcal{G}_{\text{sur}}$ are small in comparison to $\mathcal{G}_{\text{int}}$. Therefore, $\mathcal{G}$ is still considered mesh independent.

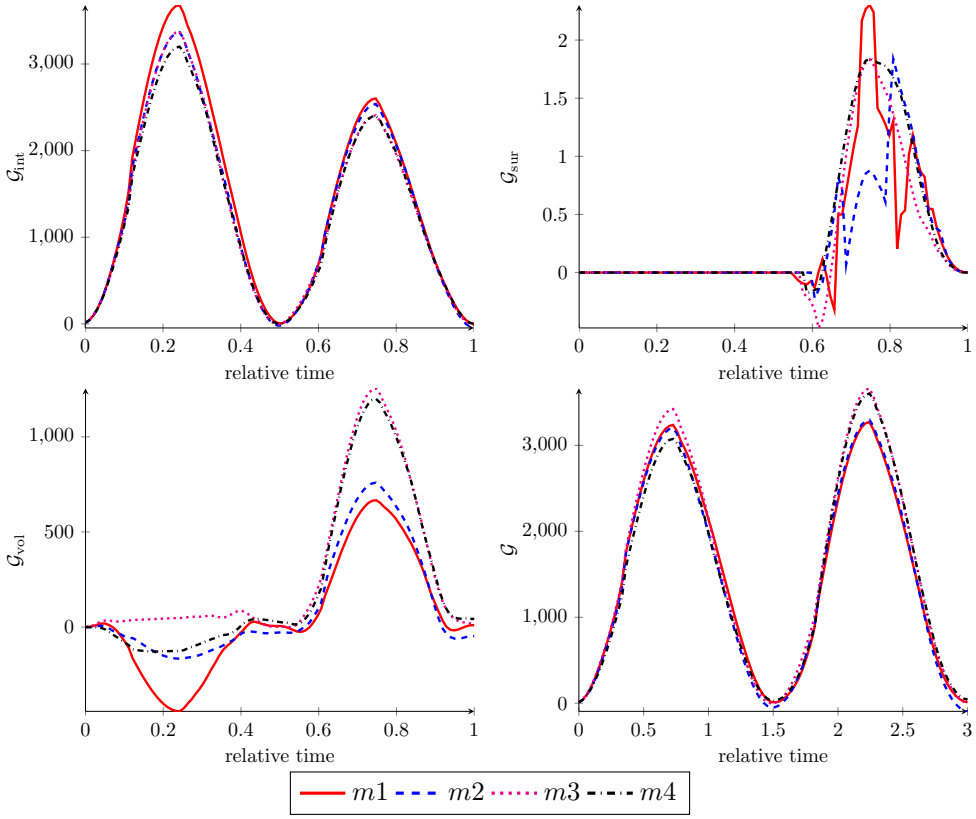

Figure 4.3: *Alternating tension–compression, inclined crack, $a_0 = 1$ mm, $\varphi = 20$ deg. Components of the material force with a linear mixed hardening material model for different mesh densities.*

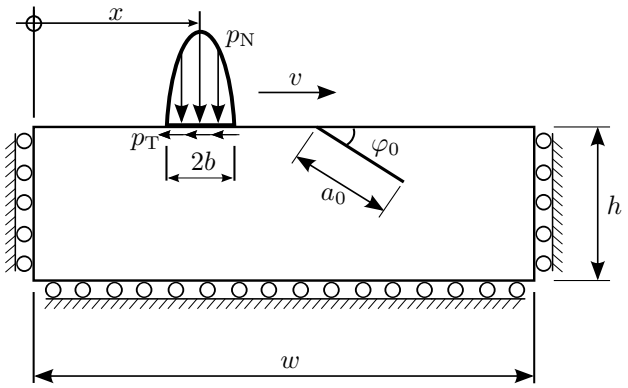

Figure 4.4: *Problem geometry and boundary conditions.*

4.2.2 Linear mixed hardening – inclined crack ($\varphi = 20°$)

From figure 4.6 it is seen that $\mathcal{G}_{\text{sur}}$ is highly unstable; however, the magnitudes are still small compared to $\mathcal{G}_{\text{int}}$. Furthermore, it is noted that the magnitude of $\mathcal{G}_{\text{vol}}$ has converged but the curve is displaced slightly. Also the magnitude after the major peak ($t \gtrsim 0.6$) is different but the effect is not very pronounced.

In general $\mathcal{G}$ will change with number of load cycles due to plastic deformations and it is, therefore, of interest to study $\mathcal{G}$ after a number of load cycles. To this end $\mathcal{G}$ is shown in Figure 4.7 after the fifth load cycle for two mesh densities. From the figure it can be seen that the maximum peak is almost the same; however, some small discrepancies are observed for the smaller peaks and there is also a small difference in the "residual-force". If a propagation law is adopted which is of a Prais' type (proportional to the range in material force $\Delta\mathcal{G}$), these small differences are not likely to influence the propagation rate significantly. Therefore, it may be concluded that in the case of RCF loading $\mathcal{G}$ is convergent.

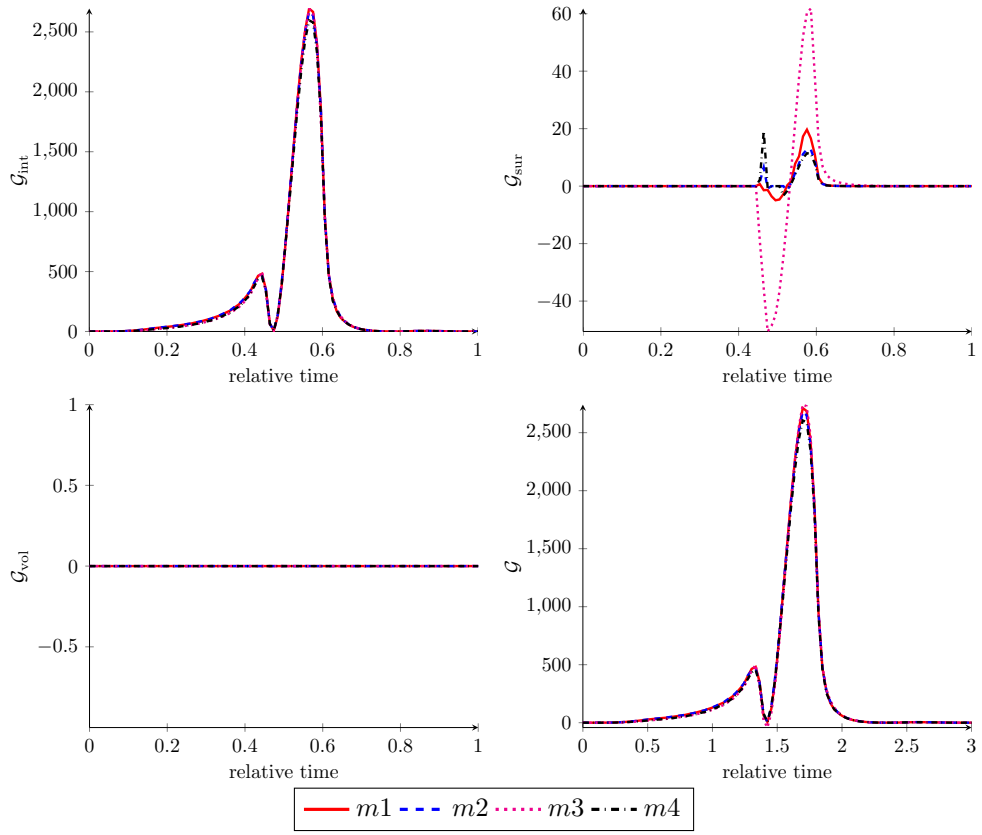

Figure 4.5: *Inclined crack, $a_0 = 1$ mm, $\varphi = 20$ deg. Components of the material force with elastic material behaviour for different mesh densities*

4.2.3 Nonlinear kinematic hardening – inclined crack ($\varphi = 20°$)

The material parameters chosen for this case are calibrated for a R260 rail grade, see [ref] for details. However, due to numerical issues (problem with obtaining convergence) isotropic hardening was artificially added, $H_{\text{iso}} = 10$ GPa. From Figure 4.8 it seen that $\mathcal{G}_{\text{vol}}$ do not converge for increased mesh density which is also reflected in the graphs of $\mathcal{G}$. Furthermore, the typical unstable behaviour of $\mathcal{G}_{\text{sur}}$ is again observed but do not give a significant contribution to $\mathcal{G}$.

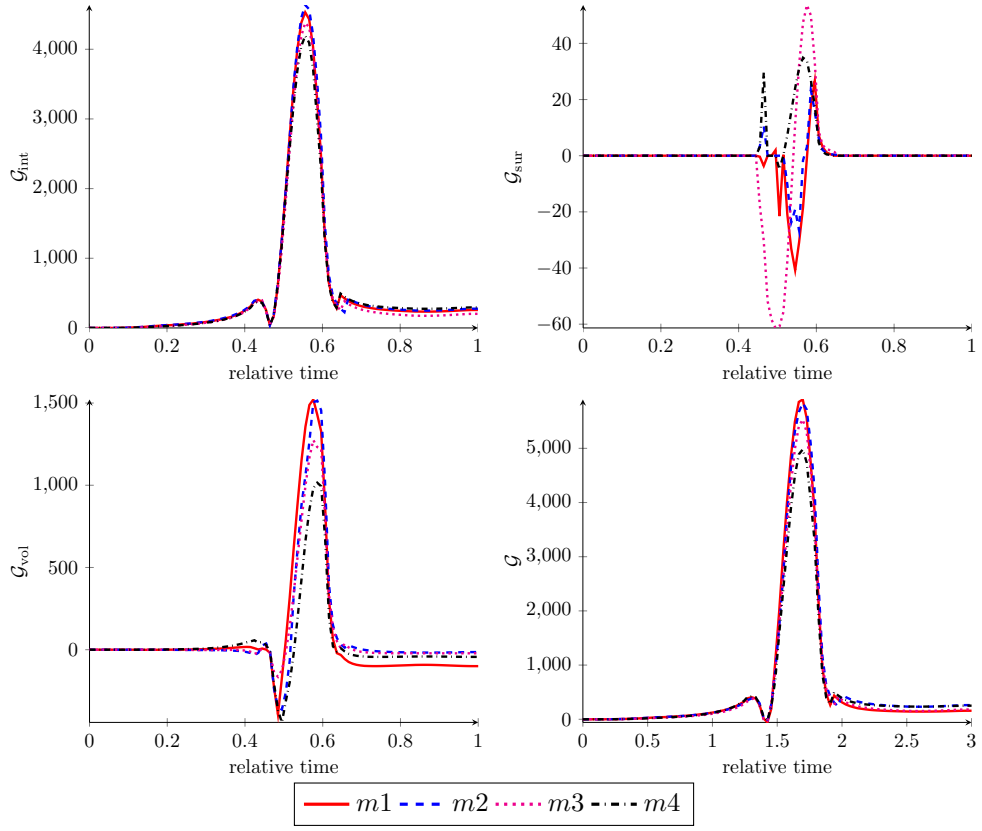

Figure 4.6: *Inclined crack, $a_0 = 1$ mm, $\varphi = 20$ deg. Components of the material force under RCF loading conditions with elasticplastic material behaviour for different mesh densities*

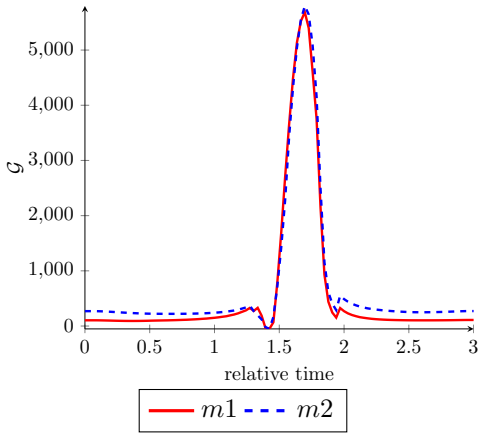

Figure 4.7: *Inclined crack, $a_0 = 1$ mm, $\varphi = 20$ deg. $\mathcal{G}$ after cycle 5 with linear mixed hardening for two mesh densities.*

4.2.4 Nonlinear kinematic hardening – vertical crack ($\varphi = 90°$)

In order to investigate whether the mesh sensitive results obtained for nonlinear kinematic hardening is sole due to the material model another crack configuration is studied. In Figure 4.9, the evolution of $\mathcal{G}$ and its components are shown for a vertical crack of length $a_0 = 2$ mm. Similar to what has been seen in the previous examples $\mathcal{G}_{\text{sur}}$ is non-convergent; however in contrast to the case of an inclined crack, $\mathcal{G}$ is convergent.

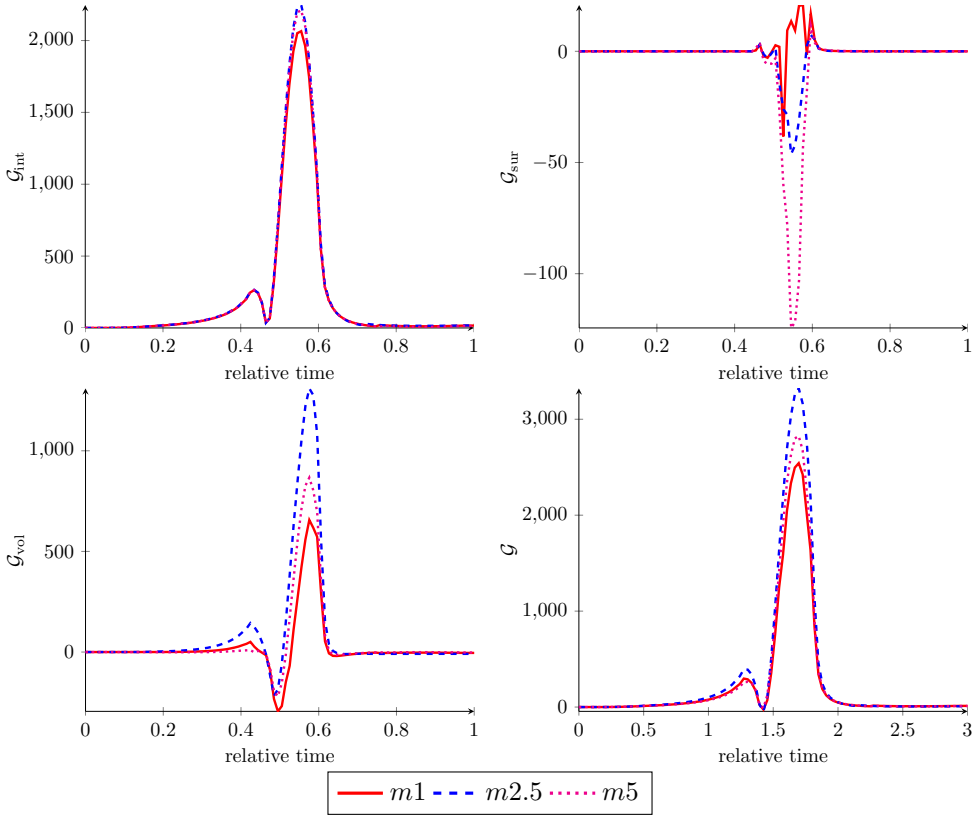

Figure 4.8: *Inclined crack, $a_0 = 1$ mm, $\varphi = 20$ deg. Components of the material force under RCF loading for nonlinear kinematic hardening.*

4.2.5 Crack growth direction

Although it was seen that $\mathcal{G}$ did not converge for increased mesh refinement for an inclined crack and with nonlinear kinematic hardening it may still be of interest to compare the direction which gives the largest crack driving force $\mathcal{G}$. This is important if a maximum energy release criterion is adopted for the prediction of propagation direction. In order to find the direction which gives the largest energy release, $\mathcal{G}$ is evaluated in different directions φ_p from the crack tip by extending the crack tip a small distance $\bar{\epsilon}$. This procedure is referred to as *probing* and is described in more detail in [1]. From these discrete evaluations of $\mathcal{G}$ the maximum in each time step may be estimated. In figure 4.10, $\mathcal{G}$ can be seen over one load cycle for 7 tested directions. It is observed that during the first peak dir 7 gives the largest $\mathcal{G}$ and during the second peak dir 1 gives the largest $\mathcal{G}$.

It is of considerable interest to investigate how plastic deformations may influence the propagation direction. Therefore, the maximum of $\mathcal{G}$, for the three studied material behaviours, are shown in Figure 4.11. From the figure it can be seen that the shapes are similar and that only the maximum peak have changed in magnitude. Moreover, this behaviour has also been observed for each individual probe direction, i.e. the behaviour for different material is as in Figure 4.10 but with different magnitudes. This implies that all the peaks correspond to the same direction (of maximum $\mathcal{G}$) which suggests that the propagation direction would be the same regardless of material behaviour. Therefore, it is concluded that the introduction of inelastic material behaviour will influence the propagation rate, due to a changes in the magnitude, but not the propagation direction.

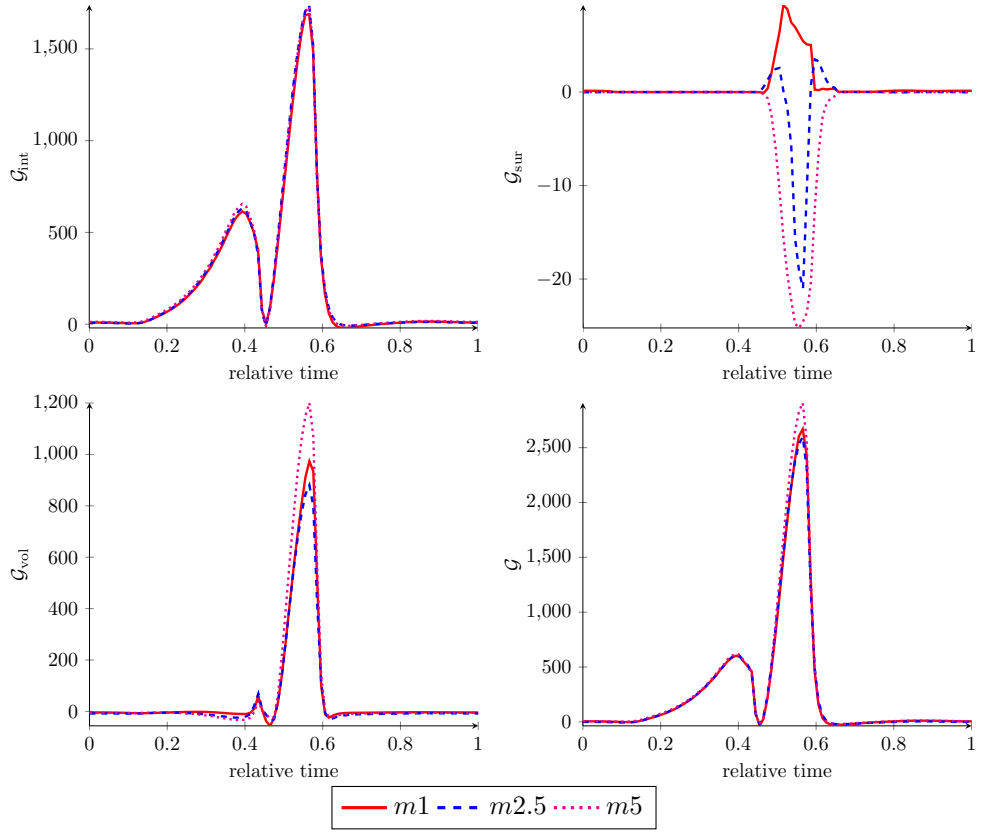

Figure 4.9: *Vertical crack, $a_0 = 2$ mm, $\varphi = 90$ deg. Components of the material force under RCF loading for nonlinear kinematic hardening.*

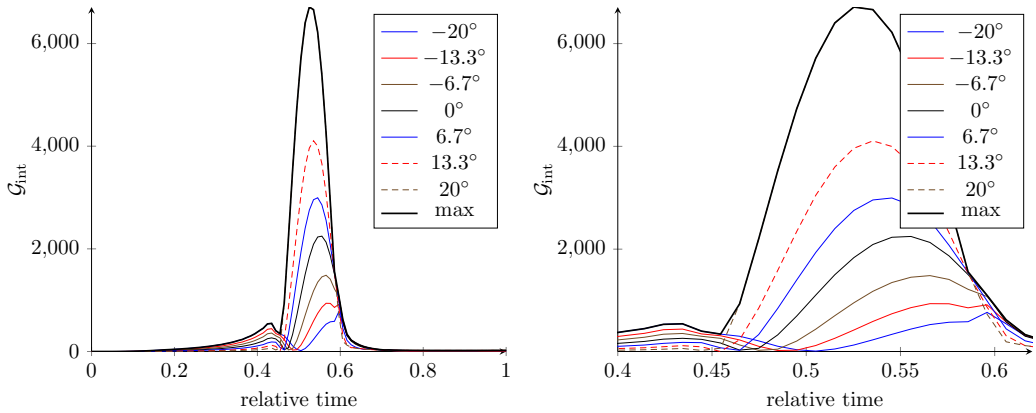

Figure 4.10: *Inclined crack, $a_0 = 1$ mm, $\varphi = 20$ deg. Material force $\mathcal{G}$ for different probe directions under RCF loading for nonlinear kinematic hardening. a) Evolution over one load cycle, b) zoom-in which shows the transition of the direction which gives the largest $\mathcal{G}$.*

4.3 Time discretization

In Figure 4.12, $\mathcal{G}_{\text{int},\parallel}$ is presented for different time discretizations of a load cycle. From the figure it is clear that 50 timesteps are enough to capture the overall behaviour of $\mathcal{G}_{\text{int},\parallel}$. But to capture the local maxima of $\mathcal{G}_{\text{int},\parallel}$, which may be important for a crack propagation law based on $\Delta\mathcal{G}$, it can be concluded that it is necessary to use 100 timesteps.

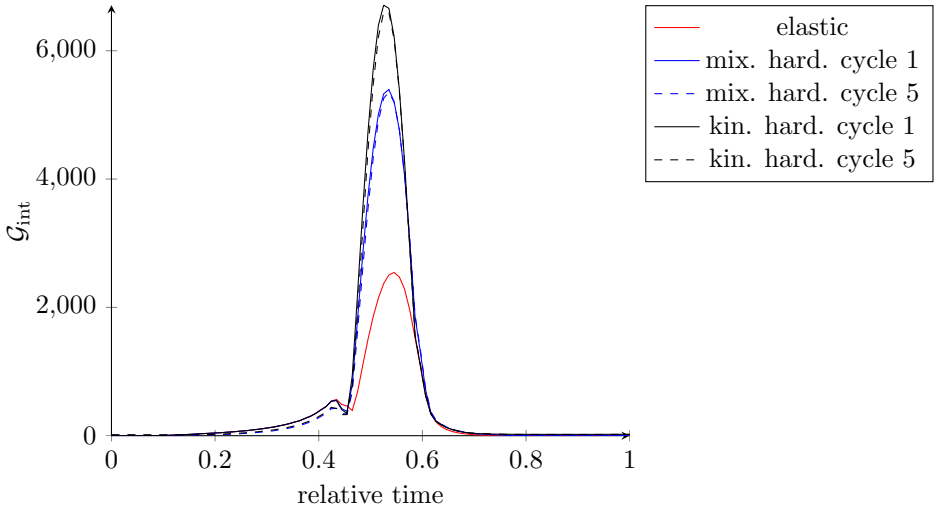

Figure 4.11: *Inclined crack, $a_0 = 1$ mm, $\varphi = 20°$. Maximum of $\mathcal{G}$ (based on different probe directions) under RCF loading compared for elasticity, linear mixed hardening and nonlinear kinematic hardening.*

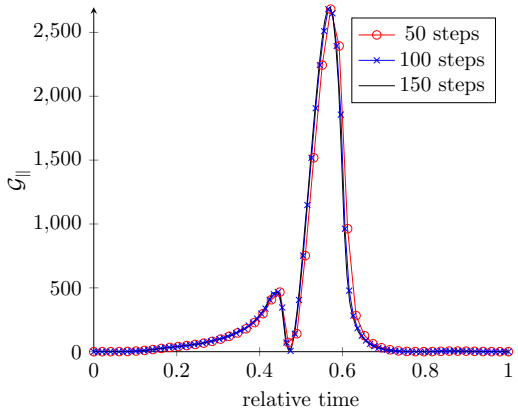

Figure 4.12: *Time history of $\boldsymbol{\mathcal{G}} \cdot \boldsymbol{e}_{\parallel}$ during a load cycle for different time discretizations.*

5 Concluding remarks and outlook

In this paper, a crack driving force for elastoplastic crack propagation is derived based on the concept of material forces. The crack driving force is evaluated for a 2D edge crack under different load cases and material behaviour. Discretization studies with focus primarily on mesh convergence leads to the follwing conclusions:

- $\mathcal{G}_{\text{sur}}$ often shows oscillatory behaviour and do generally not converge with refined mesh. However, the magnitudes are small for the load cases studied and can, therefore, be neglected.
- $\mathcal{G}$ may for the simplified load case (alternating tension-compression) be considered mesh convergent. Although the mesh convergence of $\mathcal{G}_{\text{int}}$ and $\mathcal{G}_{\text{vol}}$ individually may in some cases be questioned, $\mathcal{G}$ appears mesh convergent.
- For an inclined crack under RCF loading, with a material model with nonlinear hardening, no convergence with respect to the computational mesh was obtained. The same material response was studied for a vertical crack where it was observed that mesh convergent results were obtained.

In conclusion, the crack driving force as derived in this paper may lead to mesh dependent results for inelastic material behaviour under RCF loading conditions. Therefore, it is not a suitable quantity to use in simulation of crack growth in e.g. rails.

References

[1] J. Brouzoulis and M. Ekh. Crack propagation in rails under Rolling Contact Fatigue loading conditions based on material forces. *International Journal of Fatigue* (2012). DOI: 10.1016/j.ijfatigue.2012.06.002.

[2] R. Denzer, F. Barth, and P. Steinmann. Studies in elastic fracture mechanics based on the material force method. *International Journal for Numerical Methods in Engineering* **58**.12 (Nov. 2003), 1817–1835. ISSN: 0029-5981. DOI: 10.1002/nme.834. URL: http://doi.wiley.com/10.1002/nme.834.

[3] A. Ekberg and E. Kabo. Fatigue of railway wheels and rails under rolling contact and thermal loading—an overview. *Wear* **258**.7-8 (Mar. 2005), 1288–1300. ISSN: 00431648. DOI: 10.1016/j.wear.2004.03.039. URL: http://linkinghub.elsevier.com/retrieve/pii/S0043164804002972.

[4] F. Larsson, K. Runesson, and J. Tillberg. On the sensitivity of the rate of global energy dissipation due to configurational changes. *European Journal of Mechanics - A/Solids* **28**.6 (Nov. 2009), 1035–1050. ISSN: 09977538. DOI: 10.1016/j.euromechsol.2009.04.006. URL: http://linkinghub.elsevier.com/retrieve/pii/S099775380900059X.

[5] C. Miehe. A robust algorithm for configurational force driven brittle crack propagation with R-adaptive mesh alignment. *International Journal for Numerical Methods in Engineering* **72**.2 (2007), 127–155. DOI: 10.1002/nme. URL: http://onlinelibrary.wiley.com/doi/10.1002/nme.1999/abstract.

[6] R. Olsson and L. U., eds. *Wheel–rail interface handbook*. Woodhead Publishing Limited and CRC Press LLC, 2009. ISBN: 1 84569 412 0.

[7] A. Menzel, R. Denzer, and P. Steinmann. On the comparison of two approaches to compute material forces for inelastic materials. Application to single-slip crystal-plasticity. *Computer Methods in Applied Mechanics and Engineering* **193**.48-51 (Dec. 2004), 5411–5428. ISSN: 00457825. DOI: 10.1016/j.cma.2003.12.070. URL: http://linkinghub.elsevier.com/retrieve/pii/S0045782504002804.

[8] J. Tillberg, F. Larsson, and K. Runesson. On the role of material dissipation for the crack-driving force. *International Journal of Plasticity* **26**.7 (July 2010), 992–1012. ISSN: 07496419. DOI: 10.1016/j.ijplas.2009.12.001. URL: http://linkinghub.elsevier.com/retrieve/pii/S0749641909001624.